Charge noise and overdrive errors in reflectometry-based charge, spin and Majorana qubit readout

Vahid Derakhshan Maman, 1, * M. F. Gonzalez-Zalba, 2, † and András Pályi 1, ‡

¹Department of Theoretical Physics and MTA-BME Exotic Quantum Phases "Momentum" Research Group, Budapest University of Technology and Economics, H-1111 Budapest, Hungary
²Hitachi Cambridge Laboratory, J. J. Thomson Ave., Cambridge, CB3 0HE, United Kingdom (Dated: June 23, 2020)

Solid-state qubits incorporating quantum dots can be read out by gate reflectometry. Here, we theoretically describe physical mechanisms that render such reflectometry-based readout schemes imperfect. We discuss charge qubits, singlet-triplet spin qubits, and Majorana qubits. In our model, we account for readout errors due to slow charge noise, and due to overdriving, when a too strong probe is causing errors. A key result is that for charge and spin qubits, the readout fidelity saturates at large probe strengths, whereas for Majorana qubits, there is an optimal probe strength which provides a maximized readout fidelity. We also point out the existence of severe readout errors appearing in a resonance-like fashion as the pulse strength is increased, and show that these errors are related to probe-induced multi-photon transitions. Besides providing practical guidelines toward optimized readout, our study might also inspire ways to use gate reflectometry for device characterization.

I. INTRODUCTION

Readout of quantum bits is an essential ingredient in practical quantum computing. For quantum-dot charge qubits and spin qubits, a natural way of readout is based on charge measurements [1]. An alternative is to measure charge susceptibility, that is, the ability of a charge to be displaced when subject to a changing electrostatic environment, typically the gate voltage of a nearby gate electrode. Recent works are pointing to the possibility of applying those measurements to hybrid superconductor-semiconductor devices, potentially serving as topological quantum bits based on Majorana zero modes [2–7].

Here, we provide a theoretical analysis of qubit readout errors specific to the readout method known as reflectometry-based dispersive readout. In this method, the device hosting the quantum bit is embedded in a classical resonant circuit, and the impedance of the overall system is probed in a reflection as shown in Fig. 1a. The qubit influences the resonator impedance by changing its total capacitance $C_d = C_0 + C_q$, where C_0 is the resonator capacitance and C_q is the qubit-state-dependent parametric capacitance of a quantum dot that is either part of the qubit (charge qubit, spin qubit) or used as an auxiliary element enabling readout (Majorana qubit).

We describe generic error mechanisms that influence the readout of charge, spin, and Majorana qubits: amplifier noise, charge noise, and overdrive effects. Besides establishing simple models of these mechanisms, and analyzing their consequences for qubit readout, we also offer practical guidelines to optimize readout precision. Our results might also inspire new ways to utilize reflectometry for device characterization.

The rest of the paper is structured as follows. In section II, we introduce charge, spin and Majorana qubits, and review how amplifier noise reduces the readout fidelity in a gate-based dispersive readout experiment. In section III, we

describe the effect of charge noise. In section IV, we describe how overdriving affects the readout fidelity in a simplified, adiabatic model. In section V, we go beyond the adiabatic description and discuss the resonant reduction of readout fidelity originating from probe-induced multi-photon transitions in the device. Section VI provides a discussion, including open problems, and the paper is concluded in section VII. Details not required to follow the main text are delegated to the appendices.

II. PRELIMINARIES

A. Charge qubit

Here, we describe a typical gate-based dispersive readout setup, and exemplify how it works with the example of a double-dot charge qubit [8–15]. The readout circuit is shown in Fig. 1a. A radiofrequency signal of amplitude $V_{\rm in}$ and frequency $\omega/(2\pi)$ is sent through a transmission line (Z_0) to the resonator, where it is reflected, due to impedance mismatch, producing an output signal $V_{\rm out} = \Gamma V_{\rm in}$, where Γ is the reflection coefficient (which we will call 'reflectance' for short). $V_{\rm out}$ is measured, typically after cryogenic amplification, with an IQ demodulation system. The reflectance can be expressed as $\Gamma(\omega) = (Z(\omega) - Z_0)/(Z(\omega) + Z_0)$, where $Z(\omega)$ is the frequency-dependent equivalent impedance of the resonator, and its absolute value is limited: $|\Gamma| \leq 1$.

The reflectance carries information about the qubit state through the state-dependent parametric capacitance component C_q of the device. In an ideal scenario, each of the two qubit states yields well-defined and distinct reflectance values, and hence this measurement allows for perfect qubit readout. However, non-idealities, such as amplifier noise [16, 17] or on-device charge noise [18] render reflectance a random variable, and hence make the inference of the qubit state from the measured reflectance imperfect.

A simple model of the charge qubit is as follows. The qubit is formed by a single electron confined in a double quantum

^{*} vahid@phy.bme.hu

[†] mg507@cam.ac.uk

[‡] palyi@mail.bme.hu

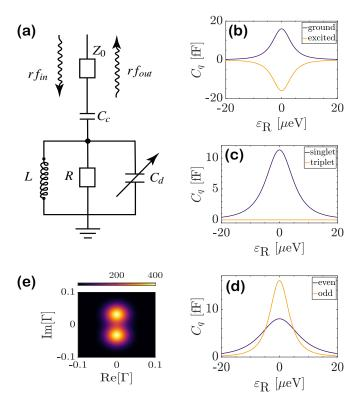


FIG. 1. Dispersive readout of charge, spin and Majorana qubits. (a) Typical circuit. The parametric capacitance C_q depending on the qubit state affects $C_d = C_0 + C_q$, hence changes the ac response of the resonant circuit. (b) C_q of the ground (purple) and excited (orange) state of a charge qubit [Eq. (3)], for $\Delta = 5\,\mu\text{eV}$. (c) C_q of the singlet (purple) and triplet (orange) state of a singlet-triplet spin qubit [Eq. (9)], for $\Delta = 5\,\mu\text{eV}$. (d) C_q of the even (purple) and odd (orange) states of a Majorana qubit [Eq. (11)], with $\Delta_{\text{even}} = 10\,\mu\text{eV}$ and $\Delta_{\text{odd}} = 5\,\mu\text{eV}$. (e) Reflectance probability distributions [Eq. (4)] due to amplifier noise for the ground (upper blob) and excited (lower blob) charge-qubit states, according to Eq. (4). Parameters: tunnel splitting: $\Delta = 5\,\mu\text{eV}$, dimensionless amplifier noise strength $\sigma_{\Gamma} = 0.02$, linear circuit response coefficient: $\alpha = 0.002\,\text{fF}^{-1}$. Overdrive effects are excluded.

dot, described by the 2×2 Hamiltonian matrix

$$H = \begin{pmatrix} 0 & \Delta/2 \\ \Delta/2 & \varepsilon_{\rm R} \end{pmatrix},\tag{1}$$

where Δ is the tunneling amplitude between the two dots, and ε_R is the detuning of the on-site energy of the right dot from that of the left dot.

To mathematically describe the readout process we make assumptions (i)-(vi) below. None of these are critical for the conclusions of our paper, we apply them only to keep the discussion focused on the most important physical effects. For more detailed discussion, see section VI and appendix A.

- (i) The resonator is directly connected to the gate electrode of the right dot.
- (ii) Among the mutual capacitances of the right dot and its surrounding metallic elements (including the left dot), the capacitance with its plunger gate dominates. This implies that

the so-called 'lever arm' parameter κ , describing the coupling of the right dot with its gate, is well approximated as $\kappa = 1$.

- (iii) The circuit is probed at its eigenfrequency corresponding to zero parametric capacitance.
- (iv) On the one hand, the integration time is much longer then a single period of the probe pulse, and the transient time scales of the resonator. On the other hand, the integration time is much shorter than the characteristic relaxation times of the system.
- (v) For simplicity, we assume that the resonator is perfectly impedance-matched to the transmission line at its resonance frequency (at zero parametric capacitance).
- (vi) Furthermore, we assume that the qubit-state-dependent parametric capacitance of the device is small, in the sense that the change in reflectance due to a change in the parametric capacitance is well approximated by a linear dependence. Together with condition (v), this implies

$$\Gamma = i\alpha C_a,\tag{2}$$

where $\alpha > 0$ is a coefficient with dimension capacitance⁻¹, whose exact value is determined by the electrical parameters of the resonator, see Appendix A for an example. Note that even without perfect impedance matching, a linear relation between Γ and C_q could be established, with a slightly modified form $\Gamma = \alpha_0 + \alpha_1 C_q$ with complex-valued α_0 and α_1 ; nevertheless, we use the simpler Eq. (2) throughout this paper.

For the charge qubit, we can associate a parametric capacitance C_q to the ground state g [10, 19], and one to the excited state e:

$$C_{q,s} = \sigma_s e^2 \frac{\Delta^2/2}{(\varepsilon_R^2 + \Delta^2)^{3/2}},\tag{3}$$

where $s \in \{g, e\}$ and $\sigma_g = +1$ and $\sigma_e = -1$. These parametric capacitances are plotted in Fig. 1b, as functions of detuning ε_R . Note that the peak parametric capacitance for a typical value of $\Delta = 5 \,\mu\text{eV}$ at the tipping point $\varepsilon_R = 0$ is $C_{q,g} \approx 16 \,\text{fF}$.

Assuming an ideal, noiseless scenario, where the readout point is the tipping point $\varepsilon_R=0$, and assuming that the quantum state to be observed is either g or e, the experimenter will measure one of the two possible reflectance values, $\Gamma_g=i\alpha C_{q,g}$ or $\Gamma_e=i\alpha C_{q,e}$. In the presence of amplifier noise, the detected reflectance becomes a random variable, with a Gaussian noise added to both quadratures. Hence the probability density function (pdf) of the reflectance for the state g reads

$$P_g(\operatorname{Re}(\Gamma),\operatorname{Im}(\Gamma)) = G(\operatorname{Re}(\Gamma),\sigma_\Gamma)G(\operatorname{Im}(\Gamma)-i\alpha C_{q,g},\sigma_\Gamma), \tag{4}$$

where $G(x,\sigma)$ is the pdf of a Gaussian random variable x with zero mean and standard deviation σ , and σ_{Γ} is the dimensionless amplifier noise strength (see below). For the state e, the reflectance pdf $P_e(\Gamma)$ has a form analogous to Eq. (4). The two-dimensional Gaussian pdfs corresponding to the states g and e are shown in Fig. 1e.

We define the dimensionless amplifier noise strength σ_{Γ} as the square root of the ratio of the amplifier noise power $P_{\rm n}$ and the input power at the resonator $P_{\rm in} = V_{\rm in}^2/Z_0$ [17, 20]. The

latter can be expressed in terms of the ac voltage amplitude at the gate of the right dot, V_{dev} , giving:

$$\sigma_{\Gamma} = \sqrt{\frac{P_{\rm n}}{P_{\rm in}}} = \frac{\sqrt{k_{\rm B}T_{\rm n}R}}{V_{\rm dev}\sqrt{t_{\rm int}}},\tag{5}$$

where $k_{\rm B}$ is Boltzmann's constant, $T_{\rm n}$ is the effective noise temperature of the amplifier, R is the resistance in the resonator (see Fig. 1a), and $t_{\rm int}$ is the integration time.

Since the reflectance is bounded, $|\Gamma| \leq 1$, a reasonable experimental setup is expected to have $\sigma_{\Gamma} \lesssim 1$. For example, for $T_{\rm n}=0.1$ K corresponding to a Josephson parametric amplifier, $R=577\,{\rm k}\Omega$ (see example circuit in appendix A), $V_{\rm dev}=10\,\mu{\rm eV}$ and $t_{\rm int}=1\,\mu{\rm s}$, we have $\sigma_{\Gamma}\approx 0.126$.

The randomness of the measured reflectance implies that the experimenter can make an erroneous inference of the qubit state based on the measured reflectance. We will characterize this readout error by two different quantities: the *signal-to-noise ratio* (SNR), which we apply only to cases where the two reflectance distributions are circularly symmetric Gaussians and have the same standard deviations, and the *readout fidelity*, which we apply generically.

As long as the measurement noise is dominated by amplifier noise, and quantum-mechanical squeezing effects[21] can be disregarded, then it is guaranteed that the two reflectance pdfs $P_g(\Gamma)$ and $P_e(\Gamma)$ are circularly symmetric two-dimensional Gaussians with identical standard deviation, as depicted in Fig. 1e. In this case, the probability of correct inference of the qubit state increases monotonically with increasing SNR, where SNR is defined as

$$SNR = \frac{|\Gamma_g - \Gamma_e|}{\sigma_{\Gamma}}.$$
 (6)

For example, we have SNR \approx 3.2, if we take the dimensionless amplifier noise strength $\sigma_{\Gamma} = 0.02$ and parametric capacitance $C_{q,g} = 16 \, \text{fF}$, and set the circuit's linear response coefficient to $\alpha = 0.002 \, \text{fF}^{-1}$, as shown in Fig. 1e.

We will see that charge noise can distort the reflectance distributions of Γ_g and Γ_e , and then the simple SNR definition in Eq. (6) is not applicable. In those cases, we will use the readout fidelity, whose definition is as follows. The starting point is the maximum likelihood inference rule. This inference rule assumes that the experimenter knows the reflectance pdfs for both qubit states from a model, and when she measures a certain reflectance value, then she will attribute it to the qubit state that has the higher probability of producing this reflectance value. Given this inference rule, the readout fidelity F is defined as the probability of correct state inference, assuming that the experimenter has zero a priori knowledge of the state. (See appendix $\bf B$ for a more detailed discussion.)

In the presence of Gaussian amplifier noise as described above, this principle translates to the following integral:

$$F = \int_{-\infty}^{\infty} d\Gamma' \int_{0}^{\infty} d\Gamma'' P_g(\Gamma', \Gamma'') = \frac{1}{2} \left[1 + \operatorname{erf}\left(\frac{\operatorname{SNR}}{2\sqrt{2}}\right) \right]. \tag{7}$$

Here, erf denotes the error function, which is a monotonically increasing function. In Eq. (7), the integral of the reflectance

imaginary part starts from zero, since, e.g., if the qubit is in state g, and we measure a reflectance with a negative imaginary part, then the inferred state is e and that is counted as a readout error. An example: with the parameter values below Eq. (6), yielding SNR ≈ 3.2 , the readout fidelity is $F \approx 0.945$.

B. Spin qubit

Now we illustrate reflectometry-based qubit readout, and the harmful effect of ampifier noise, on the example of a singlet-triplet spin qubit. For concreteness, we take the two-electron qubit based on the singlet ground state S_g and the unpolarized triplet T_0 [1, 22]. In this encoding, the parametric capacitance of the state T_0 is zero, $C_{q,T}=0$. Furthermore, the effective Hamiltonian of the singlet bonding and antibonding states in the vicinity of the (1,1) - (0,2) tipping point reads

$$H = \begin{pmatrix} U + \varepsilon_{R} & \Delta/\sqrt{2} \\ \Delta/\sqrt{2} & U + 2\varepsilon_{R} \end{pmatrix}, \tag{8}$$

where Δ is the single-electron hybridization gap, U denotes the on-site Coulomb repulsion energy, $\varepsilon_{\rm R}$ denotes the on-site energy of the right dot, the on-site energy of the left dot is set to $\varepsilon_{\rm L}=U$ for convenience, and the basis state ordering in Eq. (8) is (1,1), (0,2). Note that the (1,1)-(0,2) hybridization gap is $\Delta'=\sqrt{2}\Delta$.

Then, the parametric capacitance of the singlet ground state S_g is (cf. the relation between Eqs. (1) and (3))

$$C_{q,S} = e^2 \frac{\Delta^2}{(\varepsilon_{\rm R}^2 + 2\Delta^2)^{3/2}}.$$
 (9)

The parametric capacitances $C_{q,S}$ and $C_{q,T}$ as functions of the detuning parameter ε_R are shown in Fig. 1c.

The parametric capacitance of each qubit basis state determines the corresponding reflectance Γ_T and Γ_S via the linear circuit response approximation in Eq. (2). In the presence of amplifier noise, the SNR is defined in analogy with the charge qubit (Eq. (6)) as SNR = $|\Gamma_S - \Gamma_T|/\sigma_\Gamma$. Then, the readout fidelity formula Eq. (7) remains unchanged.

C. Majorana qubit

Finally, we discuss the case of a Majorana qubit [2, 3, 23–29]. For concreteness, we follow the description in Ref. [25], but the results generalize naturally to more recent Majorana qubit proposals, e.g., the tetron [2, 3], where charging energy protects the qubits from quasiparticle poisoning.

In the setup of Ref. [25], two Majorana zero modes γ_1 and γ_2 are coupled to an auxiliary quantum dot. This setup can be used to read out the joint parity of the two Majorana zero modes. The joint Majorana parity can also be expressed as the occupation $d^{\dagger}d$ of the nonlocal fermion $d = (\gamma_1 + i\gamma_2)/2$, so that the low-energy dynamics of the system can be studied using the occupation number basis of the readout dot and the non-local fermion, $|n_d, n_f\rangle$, where $n_d, n_f \in \{0, 1\}$.

The complex-valued tunnel coupling between the dot and γ_1 (γ_2) is denoted as v_1 (v_2), following Ref. [25]. These couplings can be tuned by adjusting barrier gate voltages and an Aharanov-Bohm flux piercing the device. The effective low-energy Hamiltonian for the even and odd sectors read

$$H_{\tau} = \frac{1}{2} \begin{pmatrix} 0 & \Delta_{\tau} \\ \Delta_{\tau} & \varepsilon_{R} \end{pmatrix}, \ \tau \in \{\text{even}, \text{odd}\}, \tag{10}$$

where $\Delta_{\rm even}=2|v_1-iv_2|$ and $\Delta_{\rm odd}=2|v_1+iv_2|$, $\varepsilon_{\rm R}$ is the on-site energy of the readout dot, and the basis states are $(e^{i\arg(v_1-iv_2)}\left|0_d,0_f\right\rangle,\left|1_d,1_f\right\rangle)$ for the even case, and $(e^{i\arg(v_1+iv_2)}\left|1_d,0_f\right\rangle,\left|0_d,1_f\right\rangle)$ for the odd case. The only difference between our Eq. (10), and Eq. (7) in Ref [25], is that we have done the above basis transformation to make the tunnel matrix elements positive ($\Delta_{\tau}>0$).

As long as the tunnel couplings v_1 and v_2 are not fine-tuned, the matrix elements Δ_{even} and Δ_{odd} are different, and the even and odd cases can be distinguished by measuring any quantity depending on Δ_{τ} , e.g., the parametric capacitance of the readout dot. This is the readout scheme we describe here. In practice, for example, one could start with the qubit decoupled from the readout dot $(v_1 = v_2 = 0)$ and with positive dot energy ε_R , either in state $|0_d, 0_f\rangle$ or $|1_d, 0_f\rangle$. Then, one can gradually (e.g., adiabatically) turn on the qubit-dot coupling and lower the dot energy such that the Hamiltonian in Eq. (10) is reached, and the state of the qubit-dot system reaches the ground state of the corresponding Hamiltonian. Then, reflectometry measures the ground-state parametric capacitance

$$C_{q,\tau} = e^2 \frac{\Delta_{\tau}^2 / 2}{(\varepsilon_{\rm p}^2(t) + \Delta_{\tau}^2)^{3/2}}.$$
 (11)

These capacitances are shown in Fig. 1d, as functions of the readout dot on-site energy ε_R , with $\Delta_{\text{even}} = 10 \,\mu\text{eV}$ and $\Delta_{\text{odd}} = 5 \,\mu\text{eV}$.

The parametric capacitances determine the reflectances Γ_{even} and Γ_{odd} via the linear circuit response approximation in Eq. (2), implying SNR = $|\Gamma_{\text{even}} - \Gamma_{\text{odd}}|/\sigma_{\Gamma}$, and with this SNR, the fidelity is still expressed as in Eq. (7).

III. CHARGE NOISE

In real qubit devices, the electromagnetic environment is not fully controlled, and hence the qubit is subject to random electromagnetic fluctuations. In many quantum-dot experiments, experimental features [30–32] are well explained by the model that the quantum-dot on-site energies slowly fluctuate, e.g., following a 1/f-type power spectrum [30, 31].

Remarkably, often the noise-induced features are captured by a *quasistatic* noise model. There, it is assumed that the on-site energies of the quantum dots change between subsequent measurement cycles, but are static within a single measurement cycle with characteristic duration $t_{\rm int}$. This is a convenient, popular, and fruitful model for typical quantum-information experiments where the experimenter has to carry out many measurement cycles to obtain a statistically accurate description of the qubit's dynamics. The success of this

quasistatic approximation can be attributed to the fact that the power spectrum of 1/f-type noise is indeed dominated by low frequencies.

Following earlier work [32–36], we will adopt the quasistatic description of charge noise in this section, and apply it to describe errors in reflectometry-based readout of the charge, spin and Majorana qubits introduced above. On the one hand, this will provide guidelines how to mitigate the noise effects that are harmful to qubit readout. On the other hand, this analysis can also be interpreted as a proposal to use the qubits as tools for charge-noise characterization.

We consider the charge qubit, add charge noise, but first, we disregard amplifier noise. Charge noise is then modelled by random components of the on-site energies of the two dots, which are assumed to be quasistatic, Gaussian, and independent of each other. Each random on-site-energy component has a standard deviation σ_c . This is equivalent to disregarding the random component of $\varepsilon_{\rm L}$ but taking a random component $\delta \varepsilon$ on $\varepsilon_{\rm R}$ with standard deviation $\sigma_{\varepsilon} = \sqrt{2}\sigma_{c}$. According to charge-qubit experiments [9, 36-40], the typical value of this charge noise strength in state-of-the-art devices ranges between $\sigma_\epsilon \sim 0.2\,\mu\text{eV}$ and $\sigma_\epsilon \sim 10\,\mu\text{eV}.$ Due to the random character of the on-site energies, the parametric capacitance will also be random, albeit not Gaussian, since the relation (3) between the detuning ε_R and the capacitance is not linear. In turn, the randomness of the parametric capacitance will carry over to the reflectance in a simple, linear fashion, at least provided that our linear-response assumption in Eq. (2) holds.

To illustrate the pdf of the measured reflectance, we numerically generate random values for $\delta \varepsilon$, and plot the resulting reflectance imaginary part $\mathrm{Im}(\Gamma)$ histograms for the ground (purple) and the excited (orange) state in Fig. 2a. As expected, based on the detuning dependence of the parametric capacitance (see Fig. 1b), and the linear relation in Eq. (2), both histograms show a sharp peak at finite $\mathrm{Im}(\Gamma)$, and a tail stretching toward zero.

In this case, the maximum likelihood inference rule implies a unit readout fidelity, F=1. This is because $\mathrm{Im}(\Gamma)=0$ is the maximum likelihood separator between the two qubit states, and the ground (excited) state always produces positive (negative) $\mathrm{Im}(\Gamma)$, hence it is impossible to make an erroneous state inference.

This perfect readout fidelity is degraded by amplifier noise, as illustrated in Fig. 2b. To generate this histogram, we randomly sample both charge noise and amplifier noise. That is, for a single realization j, the detuning is $\varepsilon_{R,j}$ and the reflectance is $\Gamma_j = \Gamma(\varepsilon_{R,j}) + \delta \Gamma'_j + i \delta \Gamma''_j$, where $\varepsilon_{R,j}$ is drawn from a Gaussian distribution with zero mean and standard deviation of σ_{ε} , whereas $\delta \Gamma'$ and $\delta \Gamma''$ are both drawn from a Gaussian distribution with zero mean and standard deviation of σ_{Γ} .

In Fig. 2b, we show a histogram that is obtained by binning the data with respect to the imaginary part of the reflectance, since in our model, amplifier- and charge-noise-induced changes in the real part do not affect the readout fidelity. This histogram is essentially a smeared version of Fig. 2a, and the smearing can be interpreted as a result of a convolution with the Gaussian representing amplifier noise.

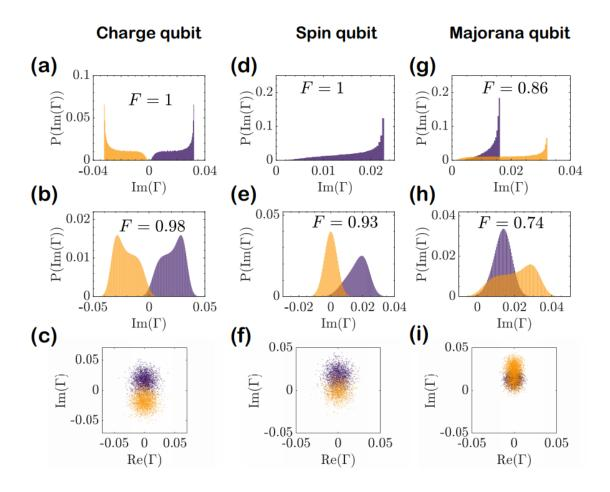


FIG. 2. Effect of charge noise and amplifier noise on the readout of charge, spin and Majorana qubits. (a) Histogram of reflectance associated to the ground (purple) and excited (orange) states for the case of charge qubit when only the charge noise is present. (b) Reflectance histogram for a charge qubit, corresponding to the ground (blue) and excited (orange) states, in the presence of both charge noise and amplifier noise. (c) Scatter plots showing the random reflectance values. (d) Spin-qubit reflectance histogram of the singlet state, with charge noise only. (The triplet case is trivial, $Im(\Gamma) = 0$ for all realizations, hence it is not shown.) (e) Spin-qubit reflectance histogram for the singlet (purple) and triplet (orange) states, with charge noise and amplifier noise. (f) Scatter plots showing the random reflectance values for the two spin-qubit basis states. (g) Majorana-qubit reflectance histogram of the even (purple) and odd (orange) ground states. (h) Majorana-qubit reflectance histogram for the even (purple) and odd (orange) ground states of the Majorana qubit, with charge and amplifier noise. (i) Scatter plots showing the random reflectance values for the two Majorana-qubit basis states. Parameters: tunneling amplitudes for the charge qubit and spin qubit: $\Delta = 5\mu eV$; for the Majorana qubit: $\Delta_{even} = 10\mu eV$ and $\Delta_{odd} = 5\mu eV$; charge noise strength: $\sigma_{\mathcal{E}} = 4\mu eV$; amplifier noise strength: $\sigma_{\Gamma} = 0.02$; linear circuit response coefficient: $\alpha = 0.002$; The histogram bin width in top panels is 4×10^{-4} . Histograms a, b, d, e, g, h are based on 100,000 realizations. Scatter plots c, f, i are based on 5,000 realizations.

To describe the picture expected for a large ensemble of measurements, we show a scatter plot of the randomly generated complex reflectance values for the ground (blue) and excited (orange) states in Fig. 2c.

We can estimate the readout fidelity corresponding to the maximum likelihood inference rule in this random sampling framework. In short, we take the bins as in Fig. 2b, and for each bin we assign an inferred state, e.g., the ground state if the bin's counts in the purple histogram is greater than the bin's counts in the orange histogram. This discretized maximum likelihood inference rule defines our readout fidelity estimate, which, in the case of the data in Fig. 2b, yields $F \approx 0.98$. The procedure for calculating F is described in detail in appendix B.

To increase the readout fidelity in an experiment, reducing both the charge noise strength σ_C and the dimensionless amplifier noise strength σ_Γ seems to be a reasonable strategy. On the one hand, σ_C is often an inherent, uncontrollable feature of the device. On the other hand, there are two ways to *in situ* reduce σ_Γ , as suggested by Eq. (5). The first way is to increase the integration time t_{int} . This might, however, imply a reduced readout fidelity due to inelastic relaxation transitions between the qubit basis states, if the integration time exceeds the characteristic relaxation time scales. (Positive consequences of charge relaxation for Majorana qubit readout are discussed in section VI.) The second way to decrease the dimensionless amplifier noise σ_Γ is to increase the amplitude of the ac probe voltage V_{dev} at the gate. As we show below in sections IV

and V, this increased probe strength induces further significant changes beyond decreasing σ_{Γ} .

We wish to emphasize that the point clouds in Fig. 2c are anisotropic: they are elongated along the imaginary axis. This feature is reminiscent of quantum noise squeezing [21]. In our case, this anisotropy is a mundane consequence of charge noise, and has nothing to do with quantum-limited amplification. We also note that an interesting application of the chargenoise-induced elongation of the reflectance distributions can be to characterize the strength σ_{ϵ} of the charge noise.

In case of the singlet-triplet spin qubit, we describe charge noise again as a quasistatic random contribution (zero mean, standard deviation σ_c) of the on-site energies of the two dots, which detunes the double dot from the (1,1)-(0,2) crossing point. Similarly to the charge-qubit case, this can be accounted for by assuming that our detuning parameter ε_R is a zero-mean Gaussian random variable with standard deviation $\sigma_{\varepsilon} = \sqrt{2\sigma_c}$. The reflectance histogram of the singlet state is shown in Fig. 2d. The triplet histogram is not shown, since the reflectance is zero in that case, irrespective of the random component of the detuning. The singlet histogram has a shape similar to that of the charge-qubit ground state in Fig. 2a. Amplifier noise causes a broadening of both peaks, as shown in the histograms of the reflectance imaginary parts in Fig. 2e, and the reflectance scatter plot in Fig. 2f. The readout fidelity calculated from the histogram of Fig. 2e is $F \approx 0.93$.

Finally, we illustrate the effect of charge noise on the readout of the Majorana qubit. Charge noise can be modelled as a random on-site energy on the readout dot [41]; we denote the corresponding standard deviation by σ_{ε} . The resulting randomness of the reflectance for the even and odd qubit states are shown in Fig. 2g. In this panel, amplifier noise is not accounted for. Remarkably, even charge noise alone makes readout imperfect (in contrast to the charge qubit and spin qubits cases), since the orange and blue histograms in Fig. 2g do overlap. We estimate the readout fidelity as F = 0.86 from the data in Fig. 2g. Accounting for amplifier noise, the reflectance pdfs are broadened, as shown in Fig. 2h, and fidelity is further reduced to $F \approx 0.74$. A remarkable feature of the Majorana qubit result in Fig. 2h is that the maximum inference rule does not yield a single threshold reflectance separating the two qubit states, but two thresholds seperating three different regions: $Im(\Gamma) < 0.005$ (even), $0.005 < Im(\Gamma) < 0.02$ (odd), and $0.02 < \text{Im}(\Gamma)$ (even).

IV. OVERDRIVE EFFECTS IN THE ADIABATIC APPROXIMATION

The results of the previous section suggest that by reducing the dimensionless amplifier noise strength σ_{Γ} , the readout fidelity is increased. According to Eq. (5), one way to reduce the σ_{Γ} is to increase the probe strength $V_{\rm dev}$. However, as we point out in this section and in the next section, the quantum dot in the device functions as a nonlinear capacitor with a $V_{\rm dev}$ -dependent effective parametric capacitance that decreases with increasing $V_{\rm dev}$. For the charge and spin qubits, this behavior can lead to a saturation of the signal-to-

noise ratio and the readout fidelity as $V_{\rm dev}$ is increased. For the Majorana qubit, this behavior implies that there is an optimal $V_{\rm dev}$ value, and increasing $V_{\rm dev}$ beyond this optimum leads to a decreasing readout fidelity. These trends, which we call 'overdrive effects', can be seen already in the adiabatic approximation, when we assume that the qubit state follows the instantaneous eigenstate of the driven qubit Hamiltonian. This section describes this adiabatic regime, whereas in the next one we incorporate probe-induced transitions into the model.

Let us take the charge qubit first, and comment on the spin and Majorana qubits later. For concreteness, we describe a scenario where the probe pulse is suddenly switched on at time t = 0, is on for an integration time t_{int} that takes a few tens or hundreds of probe periods, and then suddenly switched off. During this integration time, the double dot, tuned to the tipping point $\varepsilon_R = 0$ as the readout position, and subject to the probe pulse, is described by the Hamiltonian

$$H(t) = \begin{pmatrix} 0 & \Delta/2 \\ \Delta/2 & \varepsilon_{R}(t) \end{pmatrix}. \tag{12}$$

The time-dependent parameter $\varepsilon(t)$ represents the probe pulse:

$$\varepsilon_{\rm R}(t) = eV_{\rm dev} \sin \omega t \text{ (for } 0 < t < t_{\rm int}),$$
 (13)

with amplitude eV_{dev} , and angular frequency ω . We assume that the integration time t_{int} is much longer than the resonator transient response (ring-up and ring-down times), such that the time dependence of V_{dev} can be ignored. The impact of transients can be minimised by tailored amplitude modulation of the input signal [42].

In the results below, the frequency of the probe pulse will be set to $\omega/(2\pi) = f = 325$ MHz. Note that it corresponds to an energy quantum of $hf = \hbar\omega \approx 1.35 \mu \text{eV}$, and to a probe period $T = 1/f \approx 3.07$ ns.

As long as probe-induced excitation processes and inelastic relaxation processes can be neglected, a given energy eigenstate at t=0 will stay on its own dispersion branch for the whole integration time, i.e., the time evolution remains adiabatic. For example, the charge on the right dot in the adiabatically time-evolving charge-qubit ground state is $-|e|n_R$, with

$$n_{\rm R}(\varepsilon_{\rm R}) = \frac{1}{1 + \left(\frac{\varepsilon_{\rm R}}{\Delta} + \sqrt{1 + \left(\frac{\varepsilon_{\rm R}}{\Delta}\right)^2}\right)^2},\tag{14}$$

whose the time dependence is described by substituting $\varepsilon_{\rm R}(t)$ with Eq. (13). Together with the unit-lever-arm assumption (ii) in section III, this implies that time evolution of the charge on the gate-dot capacitor is described by $|e|n_{\rm R}(\varepsilon_{\rm R}(t))$.

In turn, this implies that an effective parametric capacitance can be attributed to this gate-dot capacitor, which is the ratio of the in-phase Fourier component of the charge response and the Fourier component of the probing voltage, both taken at the probe frequency:

$$C_q = \frac{\frac{1}{t_{\text{int}}} \int_0^{t_{\text{int}}} dt |e| n_{\text{R}}(t) \sin(\omega t)}{\frac{1}{t_{\text{int}}} \int_0^{t_{\text{int}}} dt V_{\text{dev}} \sin(\omega t) \sin(\omega t)},$$
(15)

The denominator can be readily evaluated, yielding

$$C_q = \frac{2}{V_{\text{dev}}} \frac{1}{t_{\text{int}}} \int_0^{t_{\text{int}}} dt |e| n_{\text{R}}(t) \sin(\omega t). \tag{16}$$

Furthermore, in the adiabatic approximation, the charge response $n_{\rm R}(t)$ is periodic in time with period T, hence the formula can be further simplified via $t_{\rm int} \mapsto T = 2\pi/\omega$:

$$C_q = \frac{2}{V_{\text{dev}}} \frac{1}{T} \int_0^T dt |e| n_{\text{R}}(t) \sin(\omega t). \tag{17}$$

In the adiabatic approximation, we obtain an analytical result for the parametric capacitance, by performing the integral of Eq. (17) after inserting Eq. (14) and Eq. (13):

$$C_q = \frac{2|e|}{\pi V_{\text{dev}}} f_C(x), \tag{18}$$

where the dimensionless function characterizing the capacitance is defined as

$$f_C(x) = \frac{\left(1 + x^2\right) E\left(\frac{x^2}{1 + x^2}\right) - K\left(\frac{x^2}{1 + x^2}\right)}{x\sqrt{1 + x^2}},$$
 (19)

where

$$x = \frac{|e|V_{\text{dev}}}{\Delta},\tag{20}$$

furthermore, E(x) is the complete elliptic integral of the second kind, and K(x) is the complete elliptic integral of the first kind.

The function $f_C(x)$ is shown in Fig. 3. It is strictly monotonically increasing, and its asymptotics for small arguments is

$$f_C(x \ll 1) \approx \frac{\pi}{4}x,$$
 (21)

whereas for large arguments it converges to 1:

$$f_C(x \to \infty) = 1. \tag{22}$$

Due to Eq. (21), the weak-probe limit of C_q in Eq. (18) is

$$C_q(|e|V_{\text{dev}} \ll \Delta) = \frac{|e|^2}{2\Delta},\tag{23}$$

as expected from the standard (linear) parametric capacitance formula Eq. (3).

The analytical result for the probe-strength dependence of the parametric capacitance is shown in Fig. 2a, where the solid purple (orange) line corresponds to the ground (excited) state. The magnitude of the capacitance decreases with increasing probe strength, which is the consequence of the simple fact that the charge qubit is formed by a single electron, and therefore the charge on the right dot is saturated for a large gate voltage.

Using (18), we now evaluate the SNR for the charge qubit via Eqs. (6) and (2):

$$SNR = \frac{4\alpha |e|\sqrt{t_{int}}}{\pi \sqrt{k_B T_c R}} f_C(x). \tag{24}$$

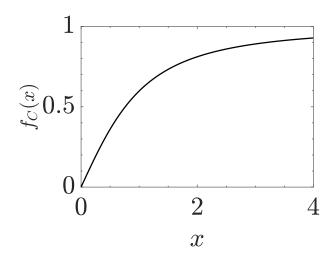


FIG. 3. The function $f_C(x)$ characterizing the probe-strength-dependence of the effective capacitance, defined in Eq. (19).

The dependence of the SNR on probe strength $V_{\rm dev}$ (via x) follows the increasing, but saturating, dependence of $f_C(x)$ on x, as illustrated in Fig. 4b, where the solid line corresponds to the adiabatic result (24). Due to Eq. (22), we conclude the best possible SNR is given by the prefactor of f_C in Eq. (24). For the example parameter set $\alpha = 0.01 \, {\rm fF}^{-1}$, $t_{\rm int} = 1 \, \mu {\rm s}$, $T_{\rm n} = 0.1 \, {\rm K}$, and $R = 577 \, {\rm k}\Omega$, we estimate a maximal signal-to-noise ratio SNR ≈ 2.29 , as seen in Fig. 4b. Correspondingly, the readout fidelity F is also saturated, see solid line in Fig. 4c.

The above paragraphs present a central result of this work: in contrast to the expectation from Eq. (5), i.e., that the readout fidelity is increasing without bounds as the probe strength $V_{\rm dev}$ is increased, here we find that the readout fidelity is saturated. The physical reason for this is that the charge response of the dot-gate capacitor is saturated for a strong probe, since there is only a single electron shuttled back and forth in the charge qubit.

It is straightforward to adapt the result (24) for the case of the singlet-triplet spin qubit, yielding

$$SNR = \frac{2\alpha |e|\sqrt{t_{int}}}{\pi\sqrt{k_B T_n R}} f_C(x'). \tag{25}$$

Note the factor of 2 difference with respect to Eq. (24), and the appearance of $x' = |e|V_{\text{dev}}/(2\sqrt{\Delta})$. We conclude that the best achievable SNR for the spin qubit is half of that for the charge qubit.

A similar calculation can be carried out for the Majorana qubit:

$$SNR = \frac{2\alpha |e|\sqrt{t_{\text{int}}}}{\pi \sqrt{k_B T_o R}} |f_C(x_{\text{odd}}) - f_C(x_{\text{even}})|, \qquad (26)$$

with $x_{\text{odd}} = |e|V_{\text{dev}}/\Delta_{\text{odd}}$ and $x_{\text{even}} = |e|V_{\text{dev}}/\Delta_{\text{even}}$. Since f_C is bounded between 0 and 1 (see Fig. 3), therefore the absolute value of the difference in Eq. (26) is also bounded between 0 and 1, as shown in Fig. 5. Therefore, we conclude that the

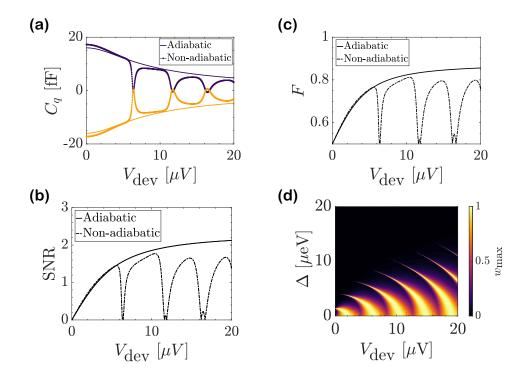


FIG. 4. Overdrive effects in reflectometry-based readout of a charge qubit. (a) Probe-strength-dependent effective parametric capacitance for ground state (purple) and excited state (orange). Solid: adiabatic approximation, Eq. (18). Points: from solution of time-dependent Schrödinger equation. (b) Signal-to-noise ratio (SNR) and (c) readout fidelity for a charge qubit, as function of probe strength, from adiabatic approximation (solid) and from time-dependent Schrödinger equation. Both (b) and (c) shows a saturation to a maximum as V_{dev} increases. (d) Maximum transition probability w_{max} as function of probe strength V_{dev} and charge-qubit hybridization gap Δ . Solid line shows the line of maximum SNR. Parameters: tunnel splitting $\Delta = 5 \,\mu\text{eV}$, detuning $\varepsilon_{\text{R}} = 0$, probe frequency: $f = 325 \,\text{MHz}$, integration time $t_{\text{int}} = 325 \,T = 1 \,\mu\text{s}$. In (b), (c): noise temperature: $T_{\text{n}} = 0.1 \,\text{K}$, linear circuit response coefficient: $\alpha = 0.01 \,\text{fF}^{-1}$, resistance $R = 577 \,\text{k}\Omega$.

best achievable SNR for the Majorana-qubit readout is given by the dimensionless fraction in Eq. (26).

A key difference of the Majorana qubit compared to the charge and spin qubits is that for the former, the SNR is opimtized by finding an appropriately chosen finite probe strength, as illustrated in Fig. 5. For example, if $\Delta_{\rm even}=10\,\mu{\rm eV}$ and $\Delta_{\rm odd}=5\,\mu{\rm eV}$, and otherwise we set the parameter values as specified in the caption of Fig. 4, then the dependence of the SNR on the probe strength follows the blue curve (n=2) in Fig. 5, implying that the best SNR is approximately $0.25\times1.14\approx0.285$, reached for $x\approx1.25$, that is, a probe strength of $V_{\rm dev}\approx1.25\,\Delta_{\rm odd}/|e|\approx6.25\,\mu{\rm V}$.

In conclusion, we have shown that for the charge and spin qubits, the adiabatic model considered here predicts a saturation of the SNR and readout fidelity as the probe strength is increased; whereas for the Majorana qubit, the same model predicts the existence of an optimal probe strength. We expect these effects to show up generically in reflectometry-based qubit-readout experiments, and to impose a theoretical upper bound on the SNR and readout fidelity. As we discuss in section VI, this effect can also be used to calibrate the amplitude $V_{\rm dev}$ of the ac voltage that reaches the gate electrode used for the reflectometry.

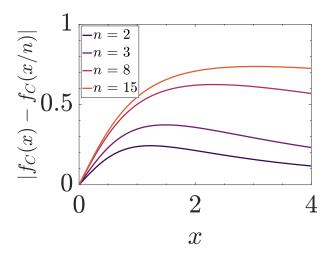


FIG. 5. Dimensionless function governing the signal-to-noise ratio of Majorana-qubit readout as function of probe strength. Second term of the right hand side of Eq. (26) is plotted, for different values of $n = \Delta_{\rm even}/\Delta_{\rm odd}$. Each curve has its unique maximum, corresponding to the best achievable signal-to-noise ratio according to Eq. (26).

V. READOUT FIDELITY REDUCTION DUE TO PROBE-INDUCED TRANSITIONS

In the previous section, we used the assumption of adiabaticity. In reality, the probe pulse is driving the system, and thereby the latter can suffer transitions from one state to another, and get driven out of the adiabatic regime. Such a transition can decrease the contrast of the measurement. Furthermore, this mechanism also induces back-action on the measured system by the measurement apparatus. Here, we focus on how the readout fidelity defined above is degraded by these probe-induced transitions.

For simplicity, we focus on the charge qubit, but the effects described here apply also to the spin and Majorana qubits. Here, we take the charge-qubit setup and Hamiltonian as defined at the beginning of section IV, but instead of applying the adiabatic approximation, we describe the system by solving the time-dependent Schrödinger equation.

Initially, the qubit is either in the ground state or in the excited state of the initial Hamiltonian $H(t = 0) = \Delta \sigma_x/2$, that is

$$|\Psi(t=0)\rangle = |\Psi_s\rangle = \frac{1}{\sqrt{2}} \begin{bmatrix} 1\\ -\sigma_s \end{bmatrix}, s \in \{g, e\}.$$
 (27)

Recall the earlier definitions $\sigma_g = +1$ and $\sigma_e = -1$. The state evolves according to the time-dependent Schrödinger equation governed by the Hamiltonian (12); we solve the Schrödinger equation numerically. This provides us with the time-evolving wave function $|\Psi(t)\rangle$, and hence the time-evolving occupation of the right dot:

$$n_{\rm R}(t) = \langle \Psi(t) | \frac{1 - \sigma_z}{2} | \Psi(t) \rangle. \tag{28}$$

Note that this function depends on the initial state being g or e. From the occupation, we calculate the probe-strength-dependent effective parametric capacitances $C_{q,g}$ and $C_{q,e}$ via Eq. (16), by performing the integral numerically. Both for the numerical solution of the Schrödinger equation and for the numerical integration, we use a time step $\Delta t = 0.001 \, T$. Finally, we determine the reflectances Γ_g and Γ_e from the effective parametric capacitances via the linear-response condition Eq. (2), and the SNR from Eq. (6).

We illustrate similarities and differences of this model, as compared to the adiabatic model of section IV, in Fig. 4. Fig. 4a shows the effective parametric capacitances for the initial state g (purple points) and e (orange points), as obtained from the numerical solution of the Schrödinger equation. The data shows the same decreasing trend with increasing probe strength $V_{\rm dev}$ as in the adiabatic case, as revealed by comparing it to the solid lines, which are the analytical results. However, there are sharp resonant dips in Fig. 4a at well-defined probe strength values, e.g., at $V_{\rm dev} \approx 6.5\,\mu\text{V}$, which are not there in the adiabatic result. These resonant features are inherited by the SNR (Fig. 4b) and by the readout fidelity (Fig. 4c). In fact, around those special, resonant values of the probe strength, readout is imprecise.

The reason for those resonant dips in the parametric capacitance, SNR and readout fidelity is the occurence of efficient

transitions between the two eigenstates of the static Hamiltonian. At these resonances, the dynamics of the qubit between its instantaneous ground and excited states resembles complete Rabi oscillations, which leads to a cancellation among the parametric capacitances of the ground and excited states which have the same absolute value but different signs.

To support this explanation, we consider g as the initial state, and calculate the maximal time-dependent transition probability over the duration of the integration time:

$$w_{\text{max}} = \max_{t \in [0, t_{\text{int}}]} |\langle \Phi_e(t) | \Psi(t) \rangle|^2.$$
 (29)

Here, $|\Phi_e(t)\rangle$ is instantaneous excited state, that is, the positive-energy eigenstate of H(t) of Eq. (12). The maximal transition probability w_{max} is plotted in Fig. 4d as the function of the probe strength V_{dev} and the tunnel splitting Δ . This panel shows separate regions of high transition probability that are bending toward the Δ axis. These regions correspond to the the dips of the SNR and readout fidelity. Each of these regions is related to a multi-photon transition: each of the regions approaches the Δ axis forming narrow 'needles', whose endpoints extrapolated to the Δ axis are $\approx 1.35 \,\mu\text{eV}$, $4.05 \,\mu\text{eV}$, $6.75 \,\mu\text{eV}$, ... accurately matching the series hf, 3hf, 5hf, ..., where f is the probe frequency. Hence, these regions correspond to probe-induced multi-photon transitions with odd photon number. Alternatively, the high-transitionprobability regions can also be interpreted as multi-passage Landau-Zener transitions [43].

Why are the even-photon transitions and the corresponding features missing from Fig. 2a-d? This is due the special multiphoton selection rules that arise because the qubit is tuned exactly to the tipping point $\varepsilon_R = 0$ in Fig. 2. Then, the probeinduced driving is described by a Hamiltonian that is transversal ($\propto \sigma_z$) to the static Hamiltonian ($\propto \sigma_x$). This restricts the active transitions to odd-photon ones[44, 45].

A further feature of Fig. 4a is that the adiabatic result and the numerical result do not match exactly at low probe strength $V_{\rm dev} \to 0$. The reason is simple: in the numerical simulation, the sinusoidal probe pulse is switched on abruptly, without a smooth envelope, hence the dynamics is not perfectly adiabatic. Note that we use this model due to its simplicity: in an experiment, the finite ring-up time of the resonator will ensure a smooth switch-on of the probe pulse and hence mitigate non-adiabatic features.

Above, we have described the probe-induced resonant dips in the readout fidelity, seen in Fig. 4c. Then it is natural to ask how these features change in the presence of charge noise? They do change, in two respects (not shown): (i) charge noise leads to the broadening of the resonant dips, and (ii) it also leads to the appearance of extra dips.

Feature (i) is rather natural: quasistatic charge noise introduces a small randomness in the qubit splitting, and hence it slightly shifts the resonance positions. Averaging with respect to charge-noise configurations hence leads to a broadening of the resonant dips.

Feature (ii) is explained as a consequence of the fact that the selection rule for the probe-induced multi-photon transitions is markedly changed when charge noise detunes the readout

point from the tipping point. Then, the transversality condition described above does not hold anymore, therefore evenphoton transitions are also activated.

VI. DISCUSSION

(1) Effects of relaxation processes. We comment on the validity of these results in the presence of relaxation processes [10, 46, 47]. For the charge qubit, our results hold if the qubit relaxation time is longer than the integration time, but the results are not valid if qubit relaxation is fast. For example, in the zero-temperature limit, if the excited state relaxes during the integration time of the measurement, then the contrast between the two reflectance values is reduced. In case of the spin qubit, our results are adequate in the limit when uphill charge relaxation (from the singlet bonding state S_g to the singlet antibonding state) and spin relaxation take longer than the integration time.

In case of the Majorana qubit, reflectometry-based readout utilizes the ground states corresponding to the two different fermion parities. Therefore, energetically downhill charge relaxation is actually useful, not harmful [2, 27, 28]. We expect that charge relaxation enforces a behavior similar to the adiabatic limit, but being a dissipative process, it should add a resistive contribution (Sisyphus resistance) to the response of the device [46], which could be quantified by calculating the out-of-phase charge response to the ac probe signal, that is, by replacing the sine in the numerator of Eq. (15) by a cosine. In the presence of fast quasiparticle poisoning, when the parity of the coupled gubit-dot system switches due to unwanted electron exchange with the environment faster than the integration time, our description loses validity. Note that quasiparticle poisoning is expected to be slow in Majorana-qubit devices based on Coulomb-blockaded islands [2, 3].

(2) Role of the lever arms. In a typical quantum-dot device, each quantum dot is capacitively coupled to multiple metallic electrodes (gates, contacts). For example, in a double-dot charge qubit, the right dot is coupled to the plunger gate of the left dot as well. We have disregarded such cross-couplings by assumption (ii) in section II A. It is straightforward to go beyond this simplification, following, e.g., Ref. [10]. We leave that for future work, but quote one result, corresponding to a special case. When the right dot couples dominantly to its gate electrode and its source and drain electrodes, but its capacitive coupling to the left dot is negligible (see Fig. 1a of Ref. [10]) then the right dot – gate coupling can be characterized by the lever arm $0 < \kappa < 1$, and the parametric capacitance calculated in the adiabatic approximation [Eq. (18)] is modified as

$$C_q = \frac{2|e|\kappa}{\pi V_{\text{dev}}} f_C(\kappa x). \tag{30}$$

(3) Further optimization of the signal-to-noise ratio. Throughout this work, we assumed that the probe frequency is fixed at the eigenfrequency of the circuit in the absence of parametric capacitance, and that in this working point, the circuit reflectance is a linear function of the qubit-state-dependent parametric capacitance [see Eq. (2)]. These as-

sumptions are convenient, because they imply that the readout fidelity does not depend on the absolute values of the qubit-state dependent effective capacitances, only on the difference of the two capacitance values. Going beyond our approximations, as described in Appendix A, a natural question arises: how to select the probe frequency to achieve an optimal signal-to-noise ratio for qubit readout? A natural choice could be to tune the probe frequency to the eigenfrequency of the circuit whose parametric capacitance is the average of the two values corresponding to the two qubit states. Since the presence of charge noise distorts the reflectance histograms from Gaussian, we expect that finding the optimal probe frequency is a nontrivial task in general.

VII. CONCLUSIONS

We have provided a theoretical description of error mechanisms that degrade qubit readout based on gate reflectometry: slow charge noise and overdrive effects. On-device charge noise creates a broadened distribution of the parametric capacitance of the device, and thereby adds uncertainty to the measured reflectance, in addition to amplifier noise. Hence charge noise leads to a reduced readout fidelity. Overdriving, that is, applying a too strong probe pulse, can lead to a scenario in which the charge response of the quantum dot, and hence the signal-to-noise ratio and the readout fidelity, is saturated as the probe strength is increased. Remarkably, in the Majorana-qubit setting, we find that there is an optimal probe strength leading to a maximal readout fidelity. Overdriving can also cause coherent transitions between quantum states, which leads to further reduction of the readout fidelity in the form of resonant dips. We expect that our results can be conveniently applied for interpretation and design of gatereflectometry experiments. Furthermore, we think that the effects explored here can be utilized for device characterization: the anisotropy of the reflectance histograms can be used to infer the charge noise strength, whereas the overdrive effects could be used to calibrate the ac probe voltage amplitude that reaches the gate electrode.

ACKNOWLEDGMENTS

We acknowledge J. Asbóth, G. Burkard, G. Fülöp and M. Kocsis for useful discussions. This work was supported by the National Research Development and Innovation Office of Hungary within the Quantum Technology National Excellence Program (Project No. 2017-1.2.1-NKP-2017-00001), under OTKA Grants 124723, 132146 by the New National Excellence Program of the Ministry of Human Capacities, and by the BME-Nanotechnology FIKP grant (BME FIKP-NAT). MFGZ acknowledges support from the Royal Society.

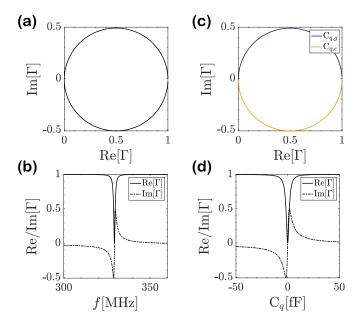


FIG. 6. Circuit reflectance as a function of probe frequency and parametric capacitance. Reflectance of the circuit shown in Fig. 1a as function of probe frequency in the absence of parametric capacitance, represented on the complex reflectance plane (a) and as a real an imaginary part (b). Reflectance of the same circuit as function of parametric capacitance, at resonant probe frequency f = 329.5 MHz, represented on the complex reflectance plane (c) and as a real and imaginary part (d). See text of Appendix A for circuit parameters.

Appendix A: An example circuit

Here, we introduce an example circuit to illustrate the key concepts that influence the physics discussed in the main text. The circuit is shown in Fig. 1a. For concreteness, we specify the circuit elements as L=405 nH, R=576.6 k Ω , $C_c=90$ fF and $C_0=486$ fF. These values are similar to those in the experiment of Ref. 11, slightly modified to obtain perfect impedance matching: at its resonance frequency f=329.5 MHz, the circuit impedance in the absence of a parametric capacitance ($C_q=0$) reads as

$$Z(\omega) = (R^{-1} + i(C_0\omega - (L\omega)^{-1}))^{-1} + (iC_c\omega)^{-1}.$$
 (A1)

This impedance is matched to a transmission-line characteristic impedance of $Z_0 = 50\Omega$. Note that perfect impedance matching is not required for reflectometry, we choose it only to simplify the discussion.

The complex reflectance of the circuit is expressed as

$$\Gamma = \frac{Z(\omega) - Z_0}{Z(\omega) + Z_0}. (A2)$$

Real and imaginary parts of the reflectance as the function of the probe frequency $f = \omega/(2\pi)$ are shown in Fig. 6b, whereas the image of the reflectance map $f \mapsto \Gamma$ is shown in Fig. 6a.

Qubit-state readout can be performed due to the dependence of the circuit impedance on the parametric capacitance

 C_q of the device containing the quantum dot(s). The qubit-state-dependent parametric capacitance modifies the device impedance via the substitution $C_0\mapsto C_0+C_q$ in Eq. (A1), which in turn changes the reflectance via Eq. (A2). For concreteness, we fix the probe frequency to the resonance circuit frequency in the absence of parametric capacitance, f=329.5 MHz, and show the dependence of the reflectance on the parametric capacitance in Fig. 6d. The image of the reflectance map $C_q\mapsto \Gamma$ is shown in Fig. 6c. The setting $C_q=0$ corresponds to the meeting point of the purple and orange arcs at $\Gamma=0$, and for small but finite C_q , the reflectance change is linear in C_q and happens along the $\mathrm{Im}(\Gamma)$ axis. For this particular circuit, a linear expansion in C_q around zero yields

$$\Gamma \approx i0.6 \, \text{fF}^{-1} C_q, \tag{A3}$$

exemplifying the general linear-response formula (2) of the main text. As illustrated by Fig. 6c, this linear relation is only approximate, and deviations from it can significantly change the results; in the main text we treat only this linear regime for simplicity, and postpone to study the role of the deviations for future work.

Appendix B: Maximum likelihood inference rule and readout fidelity

In Section III, we calculated the readout fidelities (see $F = \dots$ labels on Fig. 2a, b, d, e, g, h) of charge, spin and Majorana qubits from the reflectance histograms shown in Fig. 2. Here, we outline the procedure of that calculation.

Consider, for example, the histogram shown in Fig. 2b. Here, reflectance values Γ_j from $N_r = 100,000$ realizations in the range $-0.05 < \text{Im}(\Gamma) < 0.05$ are collected in $N_{\text{bin}} = 250$ bins, each bin with width $w_{\text{bin}} = 0.0004$. For the charge qubit ground (excited) state, the number of reflectance values in bin $i \in \{1, \dots N_{\text{bin}}\}$ is denoted as $n_i^{(g)}(n_i^{(e)})$.

With this notation, the maximum likelihood inference method is formalized as follows. When the experimenter observes a reflectance value $\operatorname{Im}(\Gamma)$ (it is sufficient to consider the imaginary part here), she picks the bin i that contains that reflectance value, compares $n_i^{(g)}$ and $n_i^{(e)}$, and infers that the qubit was in state g if $n_i^{(g)} > n_i^{(e)}$ and in state e otherwise. For later use, let us introduce the indicator function of ground-state-dominated bins $\Theta(i)$, that is, $\Theta(i) = 1$ for those bins i in which $n_i^{(g)} > n_i^{(e)}$ holds, and $\Theta(i) = 0$ for all other bin i.

Now, to characterize the accuracy of this maximum likelihood inference procedure, we just count the number of incorrect inferences, and convert that to a probability. In particular, the probability of making an incorrect inference when the charge qubit is in state g is

$$p_g = \frac{1}{N_r} \sum_{i=1}^{N_{\text{bin}}} (1 - \Theta(i)) n_i^{(g)},$$
 (B1)

whereas the probability of making an incorrect inference

when the charge qubit is in state e is

$$p_e = \frac{1}{N_r} \sum_{i=1}^{N_{\text{bin}}} \Theta(i) n_i^{(e)},$$
 (B2)

Assuming a balanced a priori probability for the two qubit

states before the measurement, we conclude that the readout fidelity is characterized by

$$F = 1 - \frac{p_g + p_e}{2}. (B3)$$

- [1] R Hanson, L P Kouwenhoven, J R Petta, S Tarucha, and L M K Vandersypen, "Spins in few-electron quantum dots," Reviews of Modern Physics **79**, 1217–1265 (2007).
- [2] Torsten Karzig, Christina Knapp, Roman M Lutchyn, Parsa Bonderson, Matthew B Hastings, Chetan Nayak, Jason Alicea, Karsten Flensberg, Stephan Plugge, Yuval Oreg, Charles M Marcus, and Michael H Freedman, "Scalable designs for quasiparticle-poisoning-protected topological quantum computation with Majorana zero modes," Physical Review B 95, 235305 (2017).
- [3] Stephan Plugge, Asbjørn Rasmussen, Reinhold Egger, and Karsten Flensberg, "Majorana box qubits," New Journal of Physics 19, 012001 (2017), 1609.01697.
- [4] Jasper van Veen, Damaz de Jong, Lin Han, Christian Prosko, Peter Krogstrup, John D Watson, Leo P Kouwenhoven, and Wolfgang Pfaff, "Revealing charge-tunneling processes between a quantum dot and a superconducting island through gate sensing," Phys. Rev. B 100, 174508 (2019).
- [5] Damaz de Jong, Jasper van Veen, Luca Binci, Amrita Singh, Peter Krogstrup, Leo P Kouwenhoven, Wolfgang Pfaff, and John D Watson, "Rapid Detection of Coherent Tunneling in an InAs Nanowire Quantum Dot through Dispersive Gate Sensing," Phys. Rev. Appl. 11, 044061 (2019).
- [6] Davydas Razmadze, Deividas Sabonis, Filip K Malinowski, Gerbold C Ménard, Sebastian Pauka, Hung Nguyen, David M.T. van Zanten, Eoin C.T. OFarrell, Judith Suter, Peter Krogstrup, Ferdinand Kuemmeth, and Charles M Marcus, "Radio-Frequency Methods for Majorana-Based Quantum Devices: Fast Charge Sensing and Phase-Diagram Mapping," Phys. Rev. Appl. 11, 064011 (2019).
- [7] Deividas Sabonis, Eoin C T O'Farrell, Davydas Razmadze, David M T van Zanten, Judith Suter, Peter Krogstrup, and Charles M Marcus, "Dispersive sensing in hybrid InAs/Al nanowires," Appl. Phys. Lett. 115, 102601 (2019).
- [8] X Mi, J V Cady, D M Zajac, P W Deelman, and J R Petta, "Strong coupling of a single electron in silicon to a microwave photon," Science 355, 156–158 (2017).
- [9] P Scarlino, D. J. van Woerkom, A Stockklauser, J. V. Koski, M. C. Collodo, S Gasparinetti, C Reichl, W Wegscheider, T Ihn, K Ensslin, and A Wallraff, "All-Microwave Control and Dispersive Readout of Gate-Defined Quantum Dot Qubits in Circuit Quantum Electrodynamics," Physical Review Letters 122, 206802 (2019).
- [10] R Mizuta, R M Otxoa, A C Betz, and M F Gonzalez-Zalba, "Quantum and tunneling capacitance in charge and spin qubits," Physical Review B 95, 045414 (2017).
- [11] Imtiaz Ahmed, James A Haigh, Simon Schaal, Sylvain Barraud, Yi Zhu, Chang-min Lee, Mario Amado, Jason W A Robinson, Alessandro Rossi, John J L Morton, and M Fernando Gonzalez-Zalba, "Radio-Frequency Capacitive Gate-Based Sensing," Physical Review Applied 10, 014018 (2018).
- [12] J. I. Colless, A. C. Mahoney, J. M. Hornibrook, A. C. Doherty, H. Lu, A. C. Gossard, and D. J. Reilly, "Dispersive Readout of a

- Few-Electron Double Quantum Dot with Fast rf Gate Sensors," Phys. Rev. Lett. **110**, 046805 (2013), 1210.4645.
- [13] M. Fernando Gonzalez-Zalba, Sergey N Shevchenko, Sylvain Barraud, J Robert Johansson, Andrew J Ferguson, Franco Nori, and Andreas C. Betz, "Gate-Sensing Coherent Charge Oscillations in a Silicon Field-Effect Transistor," Nano Lett. 16, 1614– 1619 (2016), 1602.06004.
- [14] A Stockklauser, P Scarlino, J. V. Koski, S Gasparinetti, C. K. Andersen, C Reichl, W Wegscheider, T Ihn, K Ensslin, and A Wallraff, "Strong Coupling Cavity QED with Gate-Defined Double Quantum Dots Enabled by a High Impedance Resonator," Phys. Rev. X 7, 011030 (2017).
- [15] Anasua Chatterjee, Sergey N Shevchenko, Sylvain Barraud, Rubén M Otxoa, Franco Nori, John J L Morton, and M Fernando Gonzalez-Zalba, "A silicon-based single-electron interferometer coupled to a fermionic sea," Phys. Rev. B 97, 045405 (2018).
- [16] J Stehlik, Y.-Y. Liu, C. M. Quintana, C Eichler, T. R. Hartke, and J. R. Petta, "Fast Charge Sensing of a Cavity-Coupled Double Quantum Dot Using a Josephson Parametric Amplifier," Phys. Rev. Appl. 4, 014018 (2015).
- [17] S Schaal, I Ahmed, J. A. Haigh, L Hutin, B Bertrand, S Barraud, M Vinet, C.-M. Lee, N Stelmashenko, J. W. A. Robinson, J. Y. Qiu, S Hacohen-Gourgy, I Siddiqi, M. F. Gonzalez-Zalba, and J. J. L. Morton, "Fast Gate-Based Readout of Silicon Quantum Dots Using Josephson Parametric Amplification," Phys. Rev. Lett. 124, 067701 (2020).
- [18] L Petit, J. M. Boter, H. G. J. Eenink, G Droulers, M. L. V. Tagliaferri, R Li, D. P. Franke, K. J. Singh, J. S. Clarke, R. N. Schouten, V. V. Dobrovitski, L. M. K. Vandersypen, and M Veldhorst, "Spin Lifetime and Charge Noise in Hot Silicon Quantum Dot Qubits," Phys. Rev. Lett. 121, 076801 (2018).
- [19] K. D. Petersson, C. G. Smith, D. Anderson, P. Atkinson, G. A.C. Jones, and D. A. Ritchie, "Charge and spin state readout of a double quantum dot coupled to a resonator," Nano Lett. 10, 2789–2793 (2010), 1004.4047.
- [20] Erwin W Müller and S.V. Krishnaswamy, "Energy deficits in pulsed field evaporation and deficit compensated atomprobe designs," Rev. Sci. Instrum. 45, 1053–1059 (1974).
- [21] A A Clerk, M H Devoret, S M Girvin, Florian Marquardt, and R J Schoelkopf, "Introduction to quantum noise, measurement, and amplification," Rev. Mod. Phys. 82, 1155–1208 (2010).
- [22] J. R. Petta, A. C. Johnson, J. M. Taylor, E. A. Laird, A. Yacoby, M. D. Lukin, C. M. Marcus, M. P. Hanson, and A. C. Gossard, "Coherent manipulation of coupled electron spins in semiconductor quantum dots," Science 309, 2180–2184 (2005).
- [23] A Yu Kitaev, "Unpaired Majorana fermions in quantum wires," Physics-Uspekhi 44, 131–136 (2001).
- [24] Jason Alicea, Yuval Oreg, Gil Refael, Felix von Oppen, and Matthew P A Fisher, "Non-Abelian statistics and topological quantum information processing in 1D wire networks," Nature Physics 7, 412–417 (2011), 1006.4395.
- [25] Karsten Flensberg, "Non-Abelian Operations on Majorana

- Fermions via Single-Charge Control," Phys. Rev. Lett. **106**, 090503 (2011).
- [26] Kaveh Gharavi, Darryl Hoving, and Jonathan Baugh, "Readout of Majorana parity states using a quantum dot," Phys. Rev. B 94, 155417 (2016).
- [27] Christina Knapp, Torsten Karzig, Roman M Lutchyn, and Chetan Nayak, "Dephasing of Majorana-based qubits," Phys. Rev. B 97, 125404 (2018).
- [28] Morten I. K. Munk, Jens Schulenborg, Reinhold Egger, and Karsten Flensberg, "Parity-to-charge conversion in Majorana qubit readout," (2020), arXiv:2004.02123 [cond-mat.meshall].
- [29] J. F. Steiner and F. von Oppen, "Readout of Majorana qubits," (2020), arXiv:2004.02124.
- [30] Blake M Freeman, Joshua S Schoenfield, and HongWen Jiang, "Comparison of low frequency charge noise in identically patterned Si/SiO 2 and Si/SiGe quantum dots," Appl. Phys. Lett. 108, 253108 (2016).
- [31] Jun Yoneda, Kenta Takeda, Tomohiro Otsuka, Takashi Nakajima, Matthieu R. Delbecq, Giles Allison, Takumu Honda, Tetsuo Kodera, Shunri Oda, Yusuke Hoshi, Noritaka Usami, Kohei M. Itoh, and Seigo Tarucha, "A quantum-dot spin qubit with coherence limited by charge noise and fidelity higher than 99.9%," Nat. Nanotechnol. 13, 102–106 (2018).
- [32] Jelmer M. Boter, Xiao Xue, Tobias S. Krhenmann, Thomas F. Watson, Vickram N. Premakumar, Daniel R. Ward, Donald E. Savage, Max G. Lagally, Mark Friesen, Susan N. Coppersmith, Mark A. Eriksson, Robert Joynt, and Lieven M. K. Vandersypen, "Spatial Noise Correlations in a Si/SiGe Two-Qubit Device from Bell State Coherences," (2019), arXiv:1906.02731 [cond-mat.mes-hall].
- [33] Xin Wang, Lev S Bishop, J.P. Kestner, Edwin Barnes, Kai Sun, and S Das Sarma, "Composite pulses for robust universal control of singlettriplet qubits," Nat. Commun. 3, 997 (2012).
- [34] Guilherme Tosi, Fahd A. Mohiyaddin, Vivien Schmitt, Stefanie Tenberg, Rajib Rahman, Gerhard Klimeck, and Andrea Morello, "Silicon quantum processor with robust long-distance qubit couplings," Nature Communications 8, 450 (2017).
- [35] T F Watson, S G J Philips, E Kawakami, D R Ward, P Scarlino, M Veldhorst, D E Savage, M G Lagally, Mark Friesen, S N Coppersmith, M A Eriksson, and L M K Vandersypen, "A programmable two-qubit quantum processor in silicon," Nature 555, 633–637 (2018).

- [36] Y Dovzhenko, J Stehlik, K D Petersson, J R Petta, H Lu, and A C Gossard, "Nonadiabatic quantum control of a semiconductor charge qubit," Phys. Rev. B 84, 161302 (2011).
- [37] J R Petta, A C Johnson, C M Marcus, M P Hanson, and A C Gossard, "Manipulation of a Single Charge in a Double Quantum Dot," Phys. Rev. Lett. 93, 186802 (2004).
- [38] K D Petersson, J R Petta, H Lu, and A C Gossard, "Quantum Coherence in a One-Electron Semiconductor Charge Qubit," Phys. Rev. Lett. 105, 246804 (2010).
- [39] Zhan Shi, C B Simmons, Daniel R Ward, J R Prance, R T Mohr, Teck Seng Koh, John King Gamble, Xian Wu, D E Savage, M G Lagally, Mark Friesen, S N Coppersmith, and M A Eriksson, "Coherent quantum oscillations and echo measurements of a Si charge qubit," Phys. Rev. B 88, 075416 (2013).
- [40] Brandur Thorgrimsson, Dohun Kim, Yuan-Chi Yang, L W Smith, C B Simmons, Daniel R Ward, Ryan H Foote, J Corrigan, D E Savage, M G Lagally, Mark Friesen, S N Coppersmith, and M A Eriksson, "Extending the coherence of a quantum dot hybrid qubit," npj Quantum Inf. 3, 32 (2017).
- [41] Gbor Szchenyi and Andrs Plyi, "Parity-to-charge conversion for readout of topological Majorana qubits," (2019), arXiv:1909.02326 [cond-mat.mes-hall].
- [42] T Walter, P Kurpiers, S Gasparinetti, P Magnard, A. Potočnik, Y Salathé, M Pechal, M Mondal, M Oppliger, C Eichler, and A Wallraff, "Rapid High-Fidelity Single-Shot Dispersive Readout of Superconducting Qubits," Phys. Rev. Appl. 7, 054020 (2017).
- [43] Sergey N. Shevchenko, S. Ashhab, and Franco Nori, "Landau-Zener-Stuckelberg interferometry," Phys. Rep. 492, 1–30 (2009), 0911.1917.
- [44] Jon H Shirley, "Solution of the Schrödinger Equation with a Hamiltonian Periodic in Time," Phys. Rev. 138, B979–B987 (1965).
- [45] Judit Romhányi, Guido Burkard, and András Pályi, "Subharmonic transitions and Bloch-Siegert shift in electrically driven spin resonance," Phys. Rev. B 92, 054422 (2015).
- [46] M. Esterli, R. M. Otxoa, and M. F. Gonzalez-Zalba, "Small-signal equivalent circuit for double quantum dots at low-frequencies," Applied Physics Letters 114, 253505 (2019).
- [47] B. D'Anjou and Guido Burkard, "Optimal dispersive readout of a spin qubit with a microwave resonator," Phys. Rev. B 100, 245427 (2019).